Sensitivity to hydrogen embrittlement of AISI 4140 steel: a numerical study on fracture toughness

Chiara Colombo[1*], Alfredo Zafra García[2], Javier Belzunce[2], Inés Fernandez Pariente[2]

[1] Politecnico di Milano, Department of Mechanical Engineering, Via La Masa 1, 20156 Milano, Italy

[2] University of Oviedo, Campus of Gijón, East building, 33203 Gijón, Spain

*Corresponding author: chiara.colombo@polimi.it

Abstract

Contamination of steel structures, working in environments where the presence of hydrogen cannot be neglected, can lead to significant degradation of mechanical properties, in particular, fracture toughness. In order to estimate the local hydrogen concentration at the crack tip and to understand the embrittlement mechanism, numerical models are important tools to support experimental tests that are quite complex to perform. This paper presents the application of a cohesive zone model, which couples diffusion and mechanical fields, to study the hydrogen embrittlement on AISI 4140 steel. The total hydrogen concentration, sum of the contents of hydrogen present in the lattice and in dislocation traps, is the quantity governing the embrittling effect. The input parameters of the model were calibrated using experimental tests performed on steel samples; then, initial lattice concentration was calibrated based on hydrogen pre-charged tests. A sensitivity analysis was proposed, discussing the effects of material, environmental and testing input parameters. The analysis confirms the capability of this numerical tool in predicting the mechanical response in presence of hydrogen, highlighting its potential to be used for practical design and assessment.

Keywords:

Hydrogen embrittlement; Traps; Cohesive zone modelling; Sensitivity analysis.

1. Introduction

Effects of hydrogen atoms penetrating into the steel lattice are always deleterious from the viewpoint of mechanical properties, resulting in the well-known hydrogen embrittlement phenomenon. In the past, the scientific literature faced this problem with wide experimental campaigns, focusing on the material–environment combinations and on the classification of the embrittling mechanisms. Among these, hydrogen-enhanced decohesion (HEDE) and hydrogen-enhanced localized plasticity (HELP), both involving diffusion and accumulation of hydrogen in highly stressed regions (for example a crack or notch tip), are the most relevant and frequently reported mechanisms regarding CrMo martensitic steels [1,2]. HEDE mechanism, also known as HID (Hydrogen-Induced Decohesion), initially described by Pfeil [3] and later studied by Gerberich [4], Troiano [5] and Oriani [6], is based in the reduction of the interatomic bonding energy between adjacent crystallographic planes, grain boundaries and other internal interfaces. HEDE assumes that the cohesive strength is reduced when a critical hydrogen concentration is reached in the process zone ahead of a crack tip, where hydrogen trapping becomes more relevant. In martensitic steels, HEDE mechanism is usually manifested as intergranular fracture, cleavage facets or decohesion along martensitic laths [7–10]. On the other hand, HELP mechanism, proposed by Birnmaun, Sofronis and collaborators [11–13] suggests that hydrogen increases dislocation mobility (by reducing the Peierls stress for dislocation movement), thus enhancing plasticity and shear decohesion along slip planes. Therefore, in contrast to the brittleness fostered by HEDE mechanism, HELP is characterized by a very localized deformation that takes place in highly stressed regions with great amounts of accumulated hydrogen. Consequently, in practice, this mechanism is usually associated to shallow and elongated dimples visible on the fracture surface. It is also worth mentioning that some research works have associated the combined action of HEDE and HELP mechanisms to the premature failure of CrMo steel specimens with internal hydrogen [14].

The influence of internal hydrogen on the fracture toughness of CrMo steels has been studied experimentally by several authors, e.g. [15–19], reporting in all the cases relevant fracture toughness reductions associated to important alterations of the operative fracture micromechanisms. The current work will focus on AISI 4140 steel (UNS G41400, standard ASTM A29/A29M-16, also known as 42CrMo4, standard EN ISO 683-2), widely used for drilling tools and wellhead equipment in the oil&gas field. ~~Regarding this steel~~Regarding this steel~~,~~ since the early work developed by Townsend [20], which demonstrated that even small amounts of hydrogen (below 1 ppm) could considerably reduce the crack growth resistance, other authors such as Chuang et al. [21] and Nagarajan et al. [22] have contributed to understand the influence of hydrogen on fatigue crack growth behaviour and hydrogen related fracture micromechanisms. Recently, Iijima et al. [23] reported a clear drop of the fracture toughness of AISI 4140 steel, with a yield strength of 700 MPa, when tested in high-pressure hydrogen gas~~fracture toughness data in presence of internal hydrogen is rather scarce~~. In particular, Zafra et al. [19] studied the influence of tempering temperature and displacement rate on J-R curves of hydrogen precharged C(T) specimens. A clear descent of the crack growth initiation parameter $J_{0.2BL}$ was reported in all the AISI 4140 steel grades, being maximum in those tempered at the lowest temperatures (with yield strengths higher than 1000 MPa) and tested with internal hydrogen under the lowest displacement rates. In those cases, the steel lost almost completely its resistance to crack growth. The authors also observed clear alterations of the failure micromechanisms: from microvoid coalescence to decohesion along martensitic laths or even generalized intergranular fracture in the hardest grades. These unquestionable manifestations of the HEDE micromechanism were associated to the combined effect of internal hydrogen and high hydrostatic stresses ahead of the crack tip. Additionally, the lower-strength steel grades studied in the aforementioned work, tempered at higher temperatures such as AISI 4140 quenched and tempered at 700ºC, presented a fracture micromechanism characterized by decohesion along martensitic laths in the crack initiation stage (0.2 mm from pre-crack front) and ~~also showed~~ elongated and shallow areas, with limited plastic deformation, ~~dimples~~ in the crack propagation stage, ~~their fracture surfaces,~~all of these clear signs of acting HEDE ~~HELP~~ micromechanism. ~~Anyway, the predominant fracture micromechanisms for crack initiation was always HEDE~~ [19]. It is worth mentioning that these observations

regarding the operative failure micromechanisms due to hydrogen, confirmed the findings of a previous work regarding tensile notch behavior of hydrogenated AISI 4140 quenched and tempered specimens [24].

Together with experimental testing, literature is facing the problem of hydrogen embrittlement also from numerical viewpoint. Indeed, experimental testing can be costly and time consuming, and even unreliable when the service condition is not fully defined or known as in the design stage. In these cases, numerical models can be useful to provide the designers with the damage behaviour and the embrittling tendency, thus helping in the best steel selection for specific hydrogen contaminated environments. Numerical approaches have been developed, starting from the works by Sofronis and McMeeking [25], Krom et al. [26] and Taha and Sofronis [27]. These works introduced the framework to couple equations of hydrogen diffusion with mechanical loading. They computed hydrogen concentration in the lattice and in the trap sites, including the effects of triaxiality and plastic strain, as a function of time ~~increment~~. Applications of these equations have been ~~then~~ extended, then, to the fracture mechanics approach, focusing on hydrogen embrittlement at the crack tip. Finite Elements (FE) works considered ~~cohesive zone models~~different numerical tools, implementing strength reduction at the crack tip based on the total hydrogen content, which is the quantity driving the material degradation. For instance, growing interest is paid to phase field modelling [28], as well as on cohesive zone models. This last one is the material degradation approach followed in the present paper. To cite ~~a few~~some works on cohesive modelling, Olden et al. [29], Brocks et al. [30], Kim et al. [31], and Raykar et al. [32], Díaz et al.[33] focused on the onset of crack propagation under static load and on steel toughness. In addition, Moriconi et al. [34], del Busto et al. [35], and Martinez-Paneda et al. [36] proposed formulations for cohesive elements to simulate fatigue crack growth. The reviews [2,37–39] are interesting summaries of these numerical approaches, and underline the attention of the scientific community to this topic, not only from the laboratory testing viewpoint but also for industrial applications and service lifetime prediction.

The present study considers the numerical implementation of Gobbi et al. [40], with a framework similar to the above mentioned numerical works~~, but with~~; the codes used in the present work are available in open source at [41]. This approach simulates mainly HEDE physical mechanism and estimates hydrogen concentration from numerically computed quantities during time increments, i.e. the hydrostatic stress gradient and the number of traps related to dislocations and plastic strain. The model is quite complex~~,~~ because many input parameters are necessary to define base material behaviour and its degradation with hydrogen, and their experimental measurement is not always feasible or easy to perform. For this reason, this paper will briefly present an overview of the main parameters affecting the crack propagation in presence of hydrogen, focusing on the specific input values for the AISI 4140 steel. Then, the work will describe the procedures to calibrate the cohesive law based on the hydrogen-free toughness test, and to estimate the effect of hydrogen content based on the hydrogen-charged toughness test. Finally, a sensitivity analysis is proposed, discussing the effects of material, environmental and testing input parameters. This analysis shows the capability of the developed numerical tool in the prediction of the mechanical response with hydrogen, useful for practical design and assessment.

2. Theoretical background

2.1 Hydrogen transportation models

According ~~with~~ to Oriani's theory [42], the concentration of hydrogen in reversible traps, C_T, is in equilibrium with the concentration of diffusible hydrogen in the lattice, C_L, i.e. in the Normal Interstitial Lattice Sites (NILS):

$$C_L = \theta_L N_L \tag{1}$$

$$C_T = \theta_T N_T \tag{2}$$

$$\frac{\theta_T}{1 - \theta_T} = \frac{\theta_L}{1 - \theta_L} K_T \tag{3}$$

where:

- θ_L is the occupancy of hydrogen in NILS;
- θ_T is the occupancy of hydrogen in trapping sites;
- N_L is the number of solvent lattice atoms, estimated as:

$$N_L = \frac{\mathcal{N}_A \beta \rho}{A_r}$$ (4)

where $\mathcal{N}_A$ is Avogadro's number, ρ is the steel density at 293K ($7.87 \cdot 10^3$ kg/m^3) and A_r is the molar mass of iron at 293K (0.0558 kg/mol). From these input values, N_L is equal to $5.1 \cdot 10^{20}$ sites/mm^3;

- N_T the number of traps per unit lattice volume;
- K_T is the equilibrium constant between lattice and trap sites:

$$K_T = exp\frac{E_B}{RT}$$ (5)

where R is the universal gas constant equal to 8.314 J/(mol·K), T is the absolute temperature (in the current work, tests are performed at room temperature, hence T=296K = 23°C) and E_B is the binding energy of microstructural hydrogen traps.

Based on these equations, ~~we can~~it is possible to state that the two main parameters characterizing traps are: 1) the trap density N_T, and 2) its binding energy E_b.

Regarding the first parameter, there are different traps where hydrogen can be stored and, in case, released. This work will focus on dislocations, and, therefore, the trap density is a local function of the equivalent plastic strain ε_p, as well as of the material. Indeed, literature reports some experimental studies evidencing this dependence of N_T. Table 1 reports a summary of some literature analytical laws extrapolated from experimental data. The laws proposed by Kumnick and Johnson [43], Huang et al. [44], Falkenberg [45] and Wang et al. [46] are based on permeation tests; on the other hand, the law proposed by Sofronis et al. [47] is obtained by assuming one trap per atomic plane threaded by a dislocation, consistent with the work by Thomas [48]. Figure 1 plots these equations. It is worth noting that the curve from Wang et al. [46] is related to a study on the effect of shot peening combined with hydrogen embrittlement; this curve is at least 6 orders of magnitude higher than all the others. This difference can be attributed to the considerable effects of high dislocation level and high residual stresses induced in the material by shot peening treatment [49,50].

Apart from this work, however, different steels have different trap densities based on their specific microstructures, as it is visible from the plot of Figure 1. Not only the initial value at ε_p=0 is different, but also their trends, which flatten at high ε_p following different laws. Focusing on the steel object of the present study, AISI 4140 quenched and tempered at 700ºC (2h), ~~we interpolated~~ available experimental data from permeation measurements at different levels of plastic strain [51] can be interpolated with the exponential function similar to other works [43,44,46]. The resulting law, given in Table 1 and used in the following numerical simulations, is in line with the one obtained by interpolating data from other authors [44]. The plot of Figure 1, together with these considerations, describes the importance of a customized N_T-ε_p law for an accurate prediction of numerical models.

Regarding the second parameter used to determine traps' influence in hydrogen embrittlement, the binding energy E_B, literature reports different values as a function of the specific steels and of their microstructures. Binding energies for similar trapping sites can be quite different because they reflect the variation in microstructure. Lower E_B values, around 20 kJ/mol are usually associated ~~to~~ with elastic stress fields surrounding dislocations [48,52–54], ~~that~~ which can be classified as weak and reversible traps. On the other hand, the highest E_B values of 60 kJ/mol correspond to grain boundary and interfaces [43,54,55], which are

classified as very strong or irreversible traps. Based on Eqs. (3) and (5), E_B value influences the trap occupancy θ_T:

$$\theta_T = \frac{K_T \cdot \dfrac{\theta_L}{1-\theta_L}}{1 + K_T \cdot \dfrac{\theta_L}{1-\theta_L}} \tag{6}$$

Indeed, θ_T dependency on E_B is embedded into K_T, as evidenced from Eq. (5). Figure 2 shows the trend of θ_T as a function of hydrogen concentration in the lattice C_L. For the considered practical C_L range (10^{-3}-10^1 wppm), traps with binding energies equal to or higher than 60 kJ/mol will be fully saturated, i.e. θ_T=1. This means that high energy traps (i.e. 60 kJ/mol) have little influence on embrittlement because hydrogen is not released at room temperature. On the other hand, E_B lower than 20 kJ/mol will be drained of hydrogen ~~catch almost no hydrogen atoms~~ because the θ_T curve flattens towards zero. Different works [25,27,56,57] showed that it is possible to implement analytical equations and numerical models with concurrent trapping at multiple sites, e.g. dislocations, grain boundaries, carbides. They proved that multiple traps can also interact to partially mitigate hydrogen embrittlement, up to their saturation [56].

In quenched and tempered CrMo martensitic steels, the main hydrogen traps are usually associated to interfaces between precipitated carbides and the ferritic matrix, martensitic lath, packets and blocks interfaces, grain boundaries and dislocations. However, based on experimental results, some authors [58,59] have considered dislocations as the governing trap site in quenched and tempered CrMo steels such as AISI 4140. ~~In fact~~Indeed, the distinction between the aforementioned traps in these steels, with very close binding energies, becomes extremely difficult with the current experimental techniques [60]. Trapping binding energies, E_b, in the range of 26-30 kJ/mol are usually assumed for dislocations in steels [61–68]. Based on the previous work by Zafra et al. [51] on hydrogen permeation of AISI 4140 quenched and tempered at 700ºC, the present study will focus on a single mean-energy type of traps, i.e. dislocations. In line with other authors [69,70], the binding energy E_B of 27 kJ/mol will be considered as a reference for these traps (Figure 2).

2.1.2 Parameters affecting C_T

Given Eqs. (1),(2),(3) describing the transport of hydrogen based on lattice and traps, it is possible to plot the dependence of C_T on the equivalent plastic strain ε_p, on the binding energy E_b and on C_L. In particular, for given values of C_L, ε_p, and at a fixed E_b, it is possible to estimate N_T from Table 1, and consequently C_T as:

$$C_T = \frac{N_T \cdot K_T \cdot C_L}{K_T \cdot C_L + N_L} \tag{7}$$

~~To visualize these dependencies in 2D plots, we fixed some parameters and obtained~~ Figure 3~~, that~~ describes with a 3D surface the dependency of C_T on C_L and ε_p, for E_b equal to 27kJ/mol.

Similarly, for given values E_b, it is possible to obtain K_T from Eq. (5), while for given values of ε_p, the number of traps N_T is estimated from Table 1. Fixing C_L, it is possible ultimately to apply Eq. (7), obtaining another 3D surface, shown in Figure 4. This plot underlines ~~shows~~ the dependency of C_T on E_b and ε_p, for C_L equal to 0.15wppm ~~in a 3D model~~. Both Figure 3 and Figure 4 report also specific isolines for constant C_T values.

These plots show that the dependency of C_T on C_L is really complex, and the choice of the N_T–ε_p law and E_b value can deeply influence the estimation of hydrogen effect in numerical simulations. A high level of plastic strain increases N_T and, hence, C_T, i.e. more hydrogen atoms will be trapped.

Figure 5 gives the direct dependency of C_T on C_L for two extreme values of ε_p. The plots show that high binding energies (e.g. >60kJ/mol) will result in a flat trend, i.e. traps are saturated independently on C_L. These data are consistent with Figure 1. On the other hand, low binding energies (e.g. <20kJ/mol) will result in a linear trend in these double-logarithmic plots. Selecting the intermediate binding energy of 27kJ/mol (solid curves of Figure 5), C_T increases linearly with C_L until it finally saturates. When considering the range of C_L between

0.1-10wppm, which is typical in many practical applications, numerical models will work in this transition region. Further comments and more general considerations on these parameters can be found in literature reviews [2,38].

2.2 Coupled diffusion-mechanical analysis

The framework of all the equations, implemented in the models that include the presence of hydrogen, is described in some literature works [38,71]. The equations governing hydrogen motion toward the crack tip and resulting in the macroscopic embrittling phenomenon are quite complex. Here, ~~we will briefly recall~~ the main formulae will be briefly recalled. In the present work, ~~we refer to~~the initial reference is the fully coupled implementation given in [40], exploiting the implementation available in [41].

The whole formulation is based on the hydrogen (mass) flux vector:

$$\boldsymbol{J}_m = -D_L \nabla C_L + \frac{D_L C_L \bar{V}_H}{RT} \nabla \sigma_h \tag{8}$$

where:

- D_L is the hydrogen diffusion coefficient through the interstitial sites at room temperature. The value of this parameter depends on the steel microstructure and on the testing temperature. A D_L value of $8.0 \cdot 10^{-4}$ mm^2/s was employed in this work, based on the electrochemical permeation tests performed on AISI 4140 quenched and tempered at 700ºC in [51];
- $\bar{V}_H$ is the partial molar volume of hydrogen. This is a constant equal to $2.0 \cdot 10^3$ mm^3/mol [72];
- σ_h is the hydrostatic stress, and $\nabla \sigma_h$ is its spatial gradient.

The framework is implemented within the FE software Abaqus (v. 2017, by Dassault Systèmes®), exploiting the parallelism between heat transfer equation and mass diffusion. This allows using the same formulation of thermo-mechanical FEs also for the diffusion-mechanical analysis. The main output of the simulations is the lattice concentration C_L, together with C_T computed from the last equation of Table 1 and based on the related discussion of Sect. 2.1. Their sum gives the total hydrogen content, C:

$$C = C_L + C_T \tag{9}$$

2.3 Cohesive Zone Modelling

In Cohesive Zone Modelling, crack advancement and progressive material damage can be simulated by cohesive elements, providing that the crack path is known as it is in the case of the C(T) specimen. Cohesive FEs follow a constitutive phenomenological law, the Traction Separation Law (TSL), that can assume different shapes. Literature numerical models implemented polynomial [35,71], smoothed trapezoidal [73], and multi-linear trapezoidal. ~~We~~ The selected shape is the latter, following ~~our~~ previous works [40,74]. The TSL is function of four main parameters: 1) the cohesive strength at the plateau, σ_0; 2) the separation at the onset of damage, δ_0; 3) the separation at the end of the plateau, δ_1; 4) the critical separation δ_F. Exploiting the tabular definition of TSL in Abaqus, no fixed ratios among separation values are set *a priori*, while stiffness and cohesive energy are dependent parameters.

Given the total hydrogen content C from Eq. (9), the TSL is decreased based on the coverage factor θ, defined from the Langmuir-McLean isotherm [75]:

$$\theta = \frac{C}{C + exp\left(\frac{-\Delta g_b^0}{RT}\right)} \tag{10}$$

where Δg_b^0 is the variation in Gibbs free energy between the microstructural interface and the bulk, equal to 30 kJ/mol, according to the work by Serebrinsky et al. [72]. From that same work, ~~we can~~it is possible to define the decreasing factor for decohesion strength k, simulating HEDE mechanism:

6

$$k = 1 - 1.0467 \cdot \theta + 0.1687 \cdot \theta^2 \qquad (11)$$

Figure 6.a shows the effect of the total hydrogen concentration C, the coverage factor θ and the decreasing factor k on the normalized trapezoidal TSL curve. Figure 6.b shows the corresponding monotonic percentage damage D as a function of the normalized separation δ/δ_F. The damage follows equations reported in [74] and it is function only of the three main separations, i.e. δ_0, δ_1 and δ_F. ~~Since we suppose~~Supposing that hydrogen has no effect on separations but only on strength, in accordance with the experimental results of [76], damage curves are not influenced by k, e.g. they are independent from C and collapse in one master curve.

3.   Experimental tests

This work is based on two types of experimental tests on AISI4140 steel quenched and tempered at 700ºC, tensile and fracture toughness tests, reported in [19,24].

Tensile tests were performed on AISI 4140 cylindrical specimens (Ø=5mm), in accordance with ASTM E8 standard. This type of tests allowed obtaining the stress-strain curve of the material, used as input for the following simulations. In particular, starting from the engineering curve, the experimental data beyond the flat yielded plateau were fit to a Hollomon hardening law (σ=1055$\varepsilon_p^{0.1264}$). This law is used to extrapolate stress values for higher strains and to obtain the true stress-strain curve shown in Figure 7.a~~, that~~. This curve, made of experimental and Hollomon-extrapolated data, was used in all the following numerical simulations. The elastic modulus and yield strength of this steel were 210000 MPa and 622 MPa, respectively [24].

Fracture toughness tests were performed on C(T) specimens (with the dimensions shown in Figure 7.b) without and with internal hydrogen [19], following ASTM E1820 standard. The specimens were pre-charged with gaseous hydrogen in a high-pressure hydrogen reactor at 450ºC and 19.5 MPa of pure hydrogen for 21 hours. For more information about the charging procedure and hydrogen content measurements, the reader is referred to [19,77].

Under this charging condition and after the removal process from the reactor, when important hydrogen losses took place, the average total hydrogen concentration is approximately 1.2 wppm (unevenly distributed). From this total concentration, measured by LECO analyzer, 0.3 wppm is deeply trapped hydrogen with high binding energies, so it is likely that it will not contribute to steel embrittlement. However, not all the remaining 0.9 wppm may be considered for the numerical simulations. Indeed, this experimental measurement was performed on cylindrical pins, with a geometry different from the C(T) specimens, and hydrogen content in C(T) specimens can be different, especially around the crack tip with free fracture surfaces, where hydrogen can flow out. ~~In addition~~Besides, this high experimental value of hydrogen content may be due also to other weaker traps, as carbides and lath's interfaces, which will diffuse quickly out of the specimen, being unable to reach the process zone. On the contrary, hydrogen reversibly trapped in dislocations, considered in the simulations, can be easily transported to the crack tip together with the interstitial or lattice hydrogen content [78].

4.   Numerical results

The focus of numerical models is the simulation of the fracture toughness tests performed on hydrogen pre-charged C(T) specimens of AISI 4140 steel quenched and tempered at 700ºC. Two models are implemented:

− the model without hydrogen is initially used for the calibration of the cohesive properties, i.e. TSL parameters;

− the model with hydrogen allows determining, after the experimental comparison, the effective hydrogen concentration in the surroundings of the crack at the beginning of the test (unknown value in most experimental works).

As a final example of practical application of this numerical approach, the paper will discuss in a sensitivity analysis the effect of some input parameters on the final fracture toughness behaviour of AISI 4140 quenched and tempered at 700ºC in presence of internal hydrogen.

For both models, the geometry used for the simulation (Figure 7.b, with the net thickness 10 mm) exploits the symmetry of the problem with related boundary conditions. The models consider a simplified geometry of the C(T) specimen, as a simple rectangle. The vertical load F is applied at the edge nodes in the hole region where pins are located. The mesh is the same as in [40,74], with a progressive refinement at the crack tip region (Figure 8). In particular, the smallest elements have a square shape with 30µm per side. The most refined region is 3mm long ahead of the crack tip; indeed, when the crack tip reaches this length (Δa=3mm), the load at the pins is decreased and the specimen can be considered failed and the simulation is stopped. The mesh consists of 9461 nodes and 7902 elements. Cohesive elements (COH2D4, according with Abaqus nomenclature) are placed in correspondence of the ligament, sharing their upper nodes with the adjacent continuum elements with plane strain formulation (CPE4RT).

4.1 TSL calibration: model without hydrogen

Calibration of TSL parameters is obtained following a trial and error procedure, following the indications of [79]. In particular, we considered as target the experimental R curve of the crack tip opening displacement (CTOD) as a function of the crack growth, Δa, obtained from the uncharged C(T) specimen, is considered as a target. The comparison considers the numerical CTOD, which is the vertical displacement of the original crack tip node, as well as its alternative estimation defined in [80], i.e. δ_5, which is the displacement of a point located 2.5 mm far from the initial crack tip along the vertical direction. The crack advances of one-element length when the vertical displacement of the underlying cohesive element is equal to δ_F; this condition corresponds to full damage D=100%.

Table 2 gives the parameters resulting from this calibration that will be used also for the simulation in the presence of hydrogen. Figure 9 shows the CTOD-Δa and δ_5-Δa curves corresponding to this set of parameters. This plot embeds the time dependency of the displacement field, and it means that the experimental testing time is matching with the numerical estimated time. Moreover, Iit is worth noting that CTOD values are almost overlapped with δ_5 ones; this means that the cohesive elements have a small effect on the surrounding continuum elements at the crack tip, in terms of local stiffness and of crack initiation and propagation.

4.2 Estimation of hydrogen content: model with hydrogen

The simulation of the toughness test performed on the C(T) specimen with internal hydrogen considers as input parameters the binding energy for dislocations E_B = 27 kJ/mol, following the initial discussion of Sect.2, and the diffusion coefficient D_L=8·10^{-4} mm^2/s, experimentally measured for this grade of AISI 4140 steel [51]. On the other hand, the initial hydrogen concentration in the lattice C_{L0} was unknown from experiments due to the equipment and setup used for these tests, as discussed in Sect.3. Indeed, although an initial average total hydrogen content of 1.2 wppm was measured using smaller samples, it is difficult to successfully extrapolate the concentration of hydrogen in the lattice in a small process zone located ahead of the crack tip of the C(T) specimen. In additionBesides, this estimation becomes even more arguable under the hypothesis that only hydrogen trapped in dislocations is considered in the numerical model. Therefore, the numerical model can help to estimate the effective initial hydrogen content, as will be discussed in this section. Other possible numerical applications can be related to the simulation of the whole desorption curves, in order to clarify the influence of different traps during the fracture toughness test, but this may be the aim of future investigations.

Figure 9 shows the experimental and numerical CTOD-Δa and δ_5-Δa trends in presence of hydrogen. These curves, both experimental and numerical, decrease in presence of hydrogen of about 25% in the crack propagation stage. This is obtained numerically because, during the load application, a highly stressed and

strained region at the crack tip raises, inducing hydrogen motion and material embrittlement. In order to consider this matching between the numerical and the experimental curves, the initial lattice hydrogen concentration, C_{L0}, has to be equal to 0.150 wppm. This results in an initial hydrogen trap concentration, C_{T0}, of 0.125 wppm, according to Figure 5.a and, hence, total initial hydrogen content of C_0=0.275 wppm.

Outputs of this simulation are hydrogen concentrations as a function of the distance from the crack tip, r (Figure 10.a). Focusing on the onset of crack propagation, i.e. in correspondence of the failure of the first cohesive element ahead of the crack tip, ~~we can state~~it is evident that that C_T and C_L experience two different trends. C_L shows a small peak at 60μm from the tip, i.e. between the second and third finite element, with ~~a~~ the following flattening up to the far-field C_{L0} value. On the other hand, C_T has a monotonic decreasing trend and becomes lower than C_L where this quantity experiences its peak. These two trends are in accordance with literature, e.g. [56,81]. It is worth noting that, based on these two curves, the total hydrogen concentration C is affected mainly by C_T at the crack tip; indeed, ~~we can state that~~ C_T ~~is~~ experiences much higher values than C_L at the first element (2.3wppm vs 0.2 wppm). For this steel grade, and according to classical theory, it could be confirmed that hydrogen trapped in dislocations, C_T, is the quantity governing the onset of crack propagation. Based on the total hydrogen content, the coverage factor θ and the decreasing factor k were evaluated respectively from Eq. (10) and Eq. (11), obtaining the trends shown in Figure 10.b. The factor k, that decreases the cohesive strength at the crack tip, is 0.67, and it is the quantity that summarizes the ultimate embrittling effect of hydrogen on this steel.

4.3   Sensitivity analysis

As evidenced in the description of the model framework and the governing equations (Sect.2.2), different input parameters are necessary; these parameters are function of the specific steel grade and its microstructure, hence of the applied thermal treatments or the thermal history applied to the steel. However, oftentimes, specific data are not available in the literature. Numerical models could be used to discuss hydrogen influence on structural performance both at the designing stage and for the assessment. For this reason, they find really practical applications when considering components or structures in hydrogen contaminated environments.

Indeed, some of the input parameters used for the simulation cannot be considered fully constant, and ~~we can focus our~~the attention can be focused to estimate their effect on the steel R-curves and on hydrogen concentration fields. The identified parameters are: 1) the lattice hydrogen diffusion coefficient D_L; 2) the hydrogen concentration C_0 present around the crack tip at the beginning of the simulation; and 3) the test time t, related to the applied test displacement rate. This section is dedicated to a sensitivity analysis of these parameters with respect to the CTOD R-curves and hydrogen concentration trends. In each block of simulations, only D_L or C_0 or t is varied, while all the other input parameters are maintained constant. The analysis discussed in the previous section~~,~~ is considered as a reference.

The diffusion coefficient varies not only as a function of the microstructure but also with the operating temperature ~~and with the operating condition~~ for in-field components in hydrogen contaminated environments. In addition, its experimental measurement is quite difficult, especially in presence of high-density trapping. Similar to the work in [82] for steel AISI 4130, ~~we selected~~ an inspection range between $8.0·10^{-3}$ and $8.0·10^{-6}$ mm^2/s is selected. Figure 11 shows the results of the sensitivity analysis performed using different D_L values.

The second parameter to consider is hydrogen concentration at the beginning of the simulation. In practical applications, this parameter can vary based on environmental conditions for operating components, as well as charge conditions for lab tests. In this last case, during experimental tests with hydrogen pre-charge, H content decreases steeply with air exposure at room temperature and cannot be measured in real-time. Only measurements on separate specimens can be carried out with dedicated H analysers; examples of H content decay as a function of time are given in [19,83]. Therefore, when performing tests on pre-charged

specimens as in the simulated example ~~we are simulating~~, there could be a variable H concentration. ~~We selected an~~The inspection range in terms of C_{L0} is selected between 0.1 and 0.5 wppm. Given the model framework, this C_{L0} input is also related to a corresponding C_{T0} value, based on the diagram of Figure 5.a, and, hence, to a total C_0 at the beginning of the simulation. Figure 12 shows the results of the sensitivity analysis performed with different C_{L0} (or total C_0) values.

The third parameter that has a significant importance when performing analyses with hydrogen is the time t. The simulation time governs crack growth rate and it depends on the experimental test displacement rate [19,84], that can be quite different between tests in labs or in real operative components. ~~In addition~~Besides, lab tests are often performed at fixed displacement rates, while real failures can occur under unknown or unmonitored conditions, e.g. due to unpredicted overloads of the structure. The performed analyses provide an overview of its effects in terms of hydrogen embrittlement. Figure 13 shows the results of the sensitivity analysis performed with different time values, t, to have a crack growth Δa=3mm. The reference curve is the one in which time to reach Δa=3mm is equal to 1240s, that corresponds to a displacement rate of the C(T) grips of 1mm/min. The investigated time interval ranges from 600s to 6000s.

4.4   Discussion

The diffusion coefficient drives the kinetics of hydrogen atoms towards the crack tip process zone, enhancing the embrittling effect of these atoms, decreasing the toughness of the steel and inducing a faster crack growth. The effects of D_L variation are function of the number of traps, because lattice and traps concentrations are always in equilibrium. For this reason, the effects of D_L changes are not linearly proportional in terms of CTOD R-curves (see Figure 11.a). Indeed, a huge decrease of 2 orders of magnitude in this parameter (from $8 \cdot 10^{-4}$ to $8 \cdot 10^{-6}$ mm^2/s) only slightly shifts the CTOD-Δa curve towards the ~~H~~hydrogen-free one, but at the same time ~~we can state that~~ a relative small increase up to 1 order of magnitude (from $8 \cdot 10^{-4}$ to $8 \cdot 10^{-3}$ mm^2/s) flattens the curve and induces significantly higher crack growth rates. Therefore, an increase in D_L could be extremely dangerous, while, in comparison, a decrease of the same parameter has little influence in this particular steel. Considering more in detail the hydrogen concentrations, C_L (Figure 11.b) and C_T (Figure 11.c) at the onset of crack propagation, ~~we can add some~~further comments can be added. Figure 11.b shows that C_L has a peak ahead of the crack tip, proportional to D_L values. This peak is located at the end of the first element (30 μm), for low values of D_L, but moves towards the second element (60 μm) for higher D_L values. ~~These are just indicative values, because a mesh refinement should be implemented to have a more precise indication of the peak position.~~ D_L also changes the distance to reach the far-field C_0 concentration of 0.150 wppm, ranging from r=0.3mm for D_L=$8.0 \cdot 10^{-6}$ mm^2/s to r=3mm for D_L=$8.0 \cdot 10^{-3}$ mm^2/s. These values identify the region around the crack tip recalling hydrogen from the surrounding lattice. Peak values of C_L are not comparable with C_T values at the crack tip. Indeed, Figure 11.c shows that, for r=0, C_T reaches a very high value, around 2.3 wppm, independently on D_L. This explains the fact that all the R-curves in presence of hydrogen, Figure 11.a, have a similar CTOD value to start crack propagation; while they differentiate with increasing Δa. In other words, C_T governs crack initiation, while C_L crack propagation.

Also hydrogen concentration plays an important role in the embrittlement of this steel, as shown in Figure 12.a. CTOD R-curves experience a notable change with a small variation of initial hydrogen content: similar to D_L, also the effect of C_0 does not follow a linear proportion, especially comparing the highest C_0 values considered in these simulations. The concentration will reach a saturation value, with an upper-limit on CTOD-Δa curves (the ~~H~~hydrogen-free curve). Considering Figure 12.b, ~~we can see that~~ the increase of hydrogen concentration has a similar effect as the increase of D_L (Figure 11.b), moving the peak from the first to the second and third elements of the mesh. This parameter affects also the distance r to reach the far-field value, from r=0.7mm for C_{L0}=0.100wppm to r=1.4mm for C_{L0}=0.500wppm, i.e. doubling the region recalling hydrogen from the lattice. Again, Figure 12.c shows that C_T values at the crack tip are much higher than C_L and do not depend on hydrogen concentration. Moving from the crack tip, C_T has a minimum (for C_{L0}=0.2-0.5), and then it follows the trend of C_L, on which it depends. This trend was barely visible in Figure

10

11.c, although present due to the model framework. The same considerations for D_L sensitivity regarding crack initiation and propagation are valid also for C_0 sensitivity.

Finally, time is another parameter influencing the results of these simulations. CTOD-Δa curves of Figure 13.a change as a function of the total simulation time, and have a resulting effect visible especially on the C_L trends shown in Figure 13.b. These simulations cover quite a wide temporal range. Increasing the simulation time, hydrogen has more time to move towards the crack tip process zone, resulting in a C_L enrichment of such region and, therefore, in the faster propagation of the crack. The increase in C_L due to time is similar to the D_L effect for the investigated values while, at the same time, t has a little effect on C_T (Figure 13.c).

The sensitivity analysis focused on these three main parameters that can vary during experimental tests, as they could be not fully under control in the lab environment or in-service condition. The results of these simulations proved that the cohesive zone model, properly tuned for AISI 4140 quenched and tempered at 700ºC, is able to appreciate the changes in the mechanical behaviour of this steel. For this reason, the developed numerical approach can be a versatile and practical tool for the design and assessment of steels loaded in hydrogen contaminated environments.

5.   Conclusions

This study described the influence of major input parameters used in the FE simulation in presence of hydrogen for the 42CrMo4 steel.

The initial focus is on the two main microstructural parameters affecting hydrogen embrittlement, i.e. 1) the law describing trap density N_T as a function of the equivalent plastic strain ε_p; and 2) the binding energy E_b. They are two key variables for the estimation of hydrogen concentration in traps C_T, and hence for the material degradation. These parameters are not easy to be experimentally determined, but this study evaluated their influence using numerical simulations; the precision of the numerical estimations can be further improved by incorporating the specific parameters of different steels.

Other numerical parameters affecting the simulation of crack propagation and the damage evolution are the traction and separation parameters of the cohesive law. In this case, the selected TSL shape is not important, while it is necessary to properly calibrate the single parameters of the curve with experimental data in the absence of hydrogen.

Finally, the sensitivity analysis investigated the effects on crack propagation in the presence of hydrogen of: 1) the diffusion coefficient D_L, i.e. material parameter; 2) the initial hydrogen concentration C_0, i.e. environmental parameter, and 3) time t, i.e. testing parameter. The coupled diffusion-mechanical model showed sensitivity to all these parameters. This evidences the importance of numerical tools to optimize the conditions for experimental tests and to estimate the embrittling tendency of the steel, provided that they are properly calibrated and validated. This numerical model, hence, can have wide potential applications in design and assessment stages, supporting the choice of the best steel for specific service environments.

References

[1]   S.P. Lynch, Hydrogen embrittlement (HE) phenomena and mechanisms, Stress Corros. Crack. Theory Pract. (2011) 90–130. https://doi.org/10.1533/9780857093769.1.90.

[2]   O. Barrera, D. Bombac, Y. Chen, T.D. Daff, E. Galindo-Nava, P. Gong, D. Haley, R. Horton, I. Katzarov, J.R. Kermode, C. Liverani, M. Stopher, F. Sweeney, Understanding and mitigating hydrogen

embrittlement of steels: a review of experimental, modelling and design progress from atomistic to continuum, J. Mater. Sci. 53 (2018) 6251–6290. https://doi.org/10.1007/s10853-017-1978-5.

[3]   L.B. Pfeil, P.R.S.L. A, The effect of occluded hydrogen on the tensile strength of iron, Proc. R. Soc. London. Ser. A, Contain. Pap. a Math. Phys. Character. 112 (1926) 182–195. https://doi.org/10.1098/rspa.1926.0103.

[4]   W.W. Gerberich, R.A. Oriani, M.J. Lji, X. Chen, T. Foecke, The necessity of both plasticity and brittleness in the fracture thresholds of iron, Philos. Mag. A Phys. Condens. Matter, Struct. Defects Mech. Prop. 63 (1991) 363–376. https://doi.org/10.1080/01418619108204854.

[5]   A. R. Troiano, The role of hydrogen and other interstitials in the mechanical behaviour of metals, Trans. ASM. 52 (1960) 54–80.

[6]   R.A. Oriani, A Mechanistic Theory of Hydrogen Embrittlement of Steels, in: Berichte Der Bunsen-Gesellschaft Fur Phys. Chemie, 1972: pp. 848–857.

[7]   Y. Takeda, C.J. McMahon, Strain Controlled Vs Stress Controlled Hydrogen Induced Fracture in a Quenched and Tempered Steel., Metall. Trans. A, Phys. Metall. Mater. Sci. 12 A (1981) 1255–1266. https://doi.org/10.1007/BF02642339.

[8]   K.A. Nibur, B.P. Somerday, C.S. Marchi, J.W. Foulk, M. Dadfarnia, P. Sofronis, The relationship between crack-tip strain and subcritical cracking thresholds for steels in high-pressure hydrogen gas, Metall. Mater. Trans. A Phys. Metall. Mater. Sci. 44 (2013) 248–269. https://doi.org/10.1007/s11661-012-1400-5.

[9]   A. Nagao, M. Dadfarnia, B.P. Somerday, P. Sofronis, R.O. Ritchie, Hydrogen-enhanced-plasticity mediated decohesion for hydrogen-induced intergranular and "quasi-cleavage" fracture of lath martensitic steels, J. Mech. Phys. Solids. 112 (2018) 403–430. https://doi.org/10.1016/j.jmps.2017.12.016.

[10]   A. Zafra, J. Belzunce, C. Rodríguez, I. Fernández-Pariente, Hydrogen embrittlement of the coarse grain heat affected zone of a quenched and tempered 42CrMo4 steel, Int. J. Hydrogen Energy. 45 (2020) 16890–16908. https://doi.org/10.1016/j.ijhydene.2020.04.097.

[11]   H.K. Birnbaum, Mechanisms Of Hydrogen Related Fracture Of Metals, (1989) 1–18.

[12]   H.K. Birnbaum, P. Sofronis, Hydrogen-enhanced localized plasticity-a mechanism for hydrogen-related fracture, Mater. Sci. Eng. A. 176 (1994) 191–202. https://doi.org/10.1016/0921-5093(94)90975-X.

[13]   I.M. Robertson, H.K. Birnbaum, P. Sofronis, Chapter 91 Hydrogen Effects on Plasticity, Elsevier, 2009. https://doi.org/10.1016/S1572-4859(09)01504-6.

[14]   M.B. Djukic, G.M. Bakic, V. Sijacki Zeravcic, A. Sedmak, B. Rajicic, The synergistic action and interplay of hydrogen embrittlement mechanisms in steels and iron: Localized plasticity and decohesion, Eng. Fract. Mech. 216 (2019) 106528. https://doi.org/10.1016/j.engfracmech.2019.106528.

[15]   M. Tvrdý, S. Havel, L. Hyspecká and K. Mazanec, Hydrogen embrittlement of CrMo and CrMoV pressure vessel steels, Int. J. Pres. Ves. Pip. 9 (1981) 355–365.

[16]   S. Çayan, Editorial Comment, J. Urol. 180 (2008) 1723. https://doi.org/10.1016/j.juro.2008.04.178.

[17]   S. Pillot, L. Coudreuse, Hydrogen-induced disbonding and embrittlement of steels used in petrochemical refining, Gaseous Hydrog. Embrittlement Mater. Energy Technol. Probl. Its Characterisation Eff. Part. Alloy Classes. (2012) 51–93. https://doi.org/10.1533/9780857093899.1.51.

[18]   C. Colombo, G. Fumagalli, F. Bolzoni, G. Gobbi, L. Vergani, Fatigue behavior of hydrogen pre-charged low alloy Cr-Mo steel, Int. J. Fatigue. 83 (2015). https://doi.org/10.1016/j.ijfatigue.2015.06.002.

[19]   A. Zafra, L.B. Peral, J. Belzunce, C. Rodríguez, Effects of hydrogen on the fracture toughness of 42CrMo4 steel quenched and tempered at different temperatures, Int. J. Press. Vessel. Pip. 171 (2019) 34–50. https://doi.org/10.1016/j.ijpvp.2019.01.020.

[20]   H.E. Townsend, Effects of zinc coatings on the stress corrosion cracking and hydrogen embrittlement of low-alloy steel, Metall. Trans. A. 6 (1975) 877–883. https://doi.org/10.1007/BF02672311.

[21]   J.H. Chuang, L.W. Tsay, C. Chen, Crack growth behaviour of heat-treated 4140 steel in air and gaseous hydrogen, Int. J. Fatigue. 20 (1998) 531–536. https://doi.org/10.1016/S0142-1123(98)00019-X.

[22]   V. Ramasagara Nagarajan, S.K. Putatunda, Influence of dissolved hydrogen on the fatigue crack growth behaviour of AISI 4140 steel, Int. J. Fatigue. 62 (2014) 236–248. https://doi.org/10.1016/j.ijfatigue.2013.04.018.

[23]   T. Iijima, H. Itoga, B. An, C. San Marchi, B.P. Somerday, Fracture Properties of a Cr-Mo Ferritic Steel in High-Pressure Gaseous Hydrogen, in: Proc. ASME 2015 Press. Vessel. Pip. Conf. Vol. 6B Mater. Fabr., Boston, Massachusetts, USA. July 19–23, 2015., 2015: pp. 1–7. https://doi.org/10.1115/pvp2015-45328.

[24]   A. Zafra, L.B. Peral, J. Belzunce, C. Rodríguez, Effect of hydrogen on the tensile properties of 42CrMo4 steel quenched and tempered at different temperatures, Int. J. Hydrogen Energy. 43 (2018) 9068–9082. https://doi.org/10.1016/j.ijhydene.2018.03.158.

[25]   P. Sofronis, R.M. McMeeking, Numerical analysis of hydrogen transport near a blunting crack tip, J. Mech. Phys. Solids. 37 (1989) 317–350. https://doi.org/10.1016/0022-5096(89)90002-1.

[26]   A.H.M. Krom, A.D. Bakker, Hydrogen trapping models in steel, Metall. Mater. Trans. B Process Metall. Mater. Process. Sci. 31 (2000) 1475–1482. https://doi.org/10.1007/s11663-000-0032-0.

[27]   A. Taha, P. Sofronis, A micromechanics approach to the study of hydrogen transport and embrittlement, Eng. Fract. Mech. 68 (2001) 803–837. https://doi.org/10.1016/S0013-7944(00)00126-0.

[28]   E. Martínez-Pañeda, A. Golahmar, C.F. Niordson, A phase field formulation for hydrogen assisted cracking, Comput. Methods Appl. Mech. Eng. 342 (2018) 742–761. https://doi.org/10.1016/j.cma.2018.07.021.

[29]   V. Olden, A. Alvaro, O.M. Akselsen, Hydrogen diffusion and hydrogen influenced critical stress intensity in an API X70 pipeline steel welded joint-Experiments and FE simulations, Int. J. Hydrogen Energy. 37 (2012) 11474–11486. https://doi.org/10.1016/j.ijhydene.2012.05.005.

[30]   W. Brocks, R. Falkenberg, I. Scheider, Coupling aspects in the simulation of hydrogen-induced stresscorrosion cracking, Procedia IUTAM. 3 (2012) 11–24. https://doi.org/10.1016/j.piutam.2012.03.002.

[31]   N.H. Kim, C.S. Oh, Y.J. Kim, K.B. Yoon, Y.W. Ma, Hydrogen-assisted stress corrosion cracking simulation using the stress-modified fracture strain model, J. Mech. Sci. Technol. 26 (2012) 2631–2638. https://doi.org/10.1007/s12206-012-0642-x.

[32]   N.R. Raykar, S.K. Maiti, R.K. Singh Raman, Modelling of mode-I stable crack growth under hydrogen assisted stress corrosion cracking, Eng. Fract. Mech. 78 (2011) 3153–3165. https://doi.org/10.1016/j.engfracmech.2011.07.013.

[33]   A. Díaz, J.M. Alegre, I.I. Cuesta, Numerical simulation of hydrogen embrittlement and local triaxiality effects in notched specimens, Theor. Appl. Fract. Mech. 90 (2017) 294–302. https://doi.org/10.1016/j.tafmec.2017.06.017.

[34]   C. Moriconi, G. Hénaff, D. Halm, Cohesive zone modeling of fatigue crack propagation assisted by

gaseous hydrogen in metals, Int. J. Fatigue. 68 (2014) 56–66. https://doi.org/10.1016/j.ijfatigue.2014.06.007.

[35]   S. del Busto, C. Betegón, E. Martínez-Pañeda, A cohesive zone framework for environmentally assisted fatigue, Eng. Fract. Mech. 185 (2017) 210–226. https://doi.org/10.1016/j.engfracmech.2017.05.021.

[36]   E. Martínez-Pañeda, S. del Busto, C. Betegón, Non-local plasticity effects on notch fracture mechanics, Theor. Appl. Fract. Mech. 92 (2017) 276–287. https://doi.org/10.1016/j.tafmec.2017.09.007.

[37]   A. Traidia, E. Chatzidouros, M. Jouiad, Review of hydrogen-assisted cracking models for application to service lifetime prediction and challenges in the oil and gas industry, Corros. Rev. 36 (2018) 323–347. https://doi.org/10.1515/corrrev-2017-0079.

[38]   L. Jemblie, V. Olden, O.M. Akselsen, A coupled diffusion and cohesive zone modelling approach for numerically assessing hydrogen embrittlement of steel structures, Int. J. Hydrogen Energy. 42 (2017) 11980–11995. https://doi.org/10.1016/j.ijhydene.2017.02.211.

[39]   A. Díaz, J.M. Alegre, I.I. Cuesta, A review on diffusion modelling in hydrogen related failures of metals, Eng. Fail. Anal. 66 (2016) 577–595. https://doi.org/10.1016/j.engfailanal.2016.05.019.

[40]   G. Gobbi, C. Colombo, S. Miccoli, L. Vergani, A fully coupled implementation of hydrogen embrittlement in FE analysis, Adv. Eng. Softw. 135 (2019). https://doi.org/10.1016/j.advengsoft.2019.04.004.

[41]   G. Gobbi, C. Colombo, S. Miccoli, L. Vergani, PoliHydra/hydra: fully coupled implementation, (2018). https://doi.org/10.5281/zenodo.1478086.

[42]   R.A. Oriani, The diffusion and trapping of hydrogen in steel, Acta Metall. 18 (1970) 147–157. https://doi.org/10.1016/0001-6160(70)90078-7.

[43]   A.J. Kumnick, H.H. Johnson, Deep trapping states for hydrogen in deformed iron, Acta Metall. 28 (1980) 33–39. https://doi.org/10.1016/0001-6160(80)90038-3.

[44]   H. Huang, W.J.D. Shaw, Hydrogen embrittlement interactions in cold-worked steel, Corrosion. 51 (1995) 30–36. https://doi.org/10.5006/1.3293573.

[45]   R. Falkenberg, Simulation von Wasserstofftransport und Rißwachstum infolge wasserstoffinduzierter Spannungsrißkorrosion mit einer Analyse der Kopplungsphanomenologie (in German), PhD Thesis, Christian-Albrechts-Universitat, Kiel, Germany, 2010.

[46]   Y. Wang, X. Wu, Z. Zhou, X. Li, Numerical analysis of hydrogen transport into a steel after shot peening, Results Phys. 11 (2018) 5–16. https://doi.org/10.1016/j.rinp.2018.08.030.

[47]   P. Sofronis, Y. Liang, N. Aravas, Hydrogen induced shear localization of the plastic flow in metals and alloys, Eur. J. Mech. A/Solids. 20 (2001) 857–872. https://doi.org/10.1016/S0997-7538(01)01179-2.

[48]   G.J. Thomas, Hydrogen Trapping in FCC Metals., (1981) 77–85.

[49]   S. Bagherifard, I. Fernandez-Pariente, R. Ghelichi, M. Guagliano, Fatigue behavior of notched steel specimens with nanocrystallized surface obtained by severe shot peening, Mater. Des. 45 (2013) 497–503. https://doi.org/10.1016/j.matdes.2012.09.025.

[50]   C. Colombo, M. Guagliano, L. Vergani, Fatigue crack growth behaviour of nitrided and shot peened specimens, SID Struct. Integr. Durab. 1 (2005) 253–265. https://doi.org/10.3970/sdhm.2005.001.253.

[51]   A. Zafra, J. Belzunce, C. Rodríguez, Hydrogen diffusion and trapping IN 42CrMo4 quenched and tempered steel: Influence of quenching temperature and plastic deformation, Mater. Chem. Phys. (2020) 123599. https://doi.org/10.1016/j.matchemphys.2020.123599.

[52]   T. Yamaguchi, M. Nagumo, Simulation of hydrogen thermal desorption under reversible trapping by

lattice defects, ISIJ Int. 43 (2003) 514–519. https://doi.org/10.2355/isijinternational.43.514.

[53] G.M. Pressouyre, I.M. Bernstein, A quantitative analysis of hydrogen trapping, Metall. Trans. A. 9 (1978) 1571–1580. https://doi.org/10.1007/BF02661939.

[54] R. Gibala and A.J. Kumnick, Hydrogen Trapping in Iron and Steels, in: R. Gibala and R.F. Hehemann (Ed.), Hydrog. Embrittlement Stress Corros. Crack., American Society for Metals, Metals Park, Ohio, Estados Unidos, 1984: pp. 61–77.

[55] D. Li, R.P. Gangloff, J.R. Scully, Hydrogen Trap States in Ultrahigh-Strength AERMET 100 Steel, Metall. Mater. Trans. A Phys. Metall. Mater. Sci. 35 A (2004) 849–864. https://doi.org/10.1007/s11661-004-0011-1.

[56] M. Dadfarnia, P. Sofronis, T. Neeraj, Hydrogen interaction with multiple traps: Can it be used to mitigate embrittlement?, Int. J. Hydrogen Energy. 36 (2011) 10141–10148. https://doi.org/10.1016/j.ijhydene.2011.05.027.

[57] W. Wu, Y. Wang, P. Tao, X. Li, J. Gong, Cohesive zone modeling of hydrogen-induced delayed intergranular fracture in high strength steels, Results Phys. 11 (2018) 591–598. https://doi.org/10.1016/j.rinp.2018.10.001.

[58] Y. Sakamoto, T. Mantani, Effect of quenching and tempering on diffusion of hydrogen in carbon steel, Trans. JIM. 17 (1976).

[59] F.G. Wei, K. Tsuzaki, Response of hydrogen trapping capability to microstructural change in tempered Fe-0.2C martensite, Scr. Mater. 52 (2005) 467–472. https://doi.org/10.1016/j.scriptamat.2004.11.008.

[60] F.G. Wei, K. Tsuzaki, Hydrogen trapping phenomena in martensitic steels, Gaseous Hydrog. Embrittlement Mater. Energy Technol. Probl. Its Characterisation Eff. Part. Alloy Classes. (2012) 493–525. https://doi.org/10.1533/9780857093899.3.493.

[61] H.K.D.H. Bhadeshia, Prevention of hydrogen embrittlement in steels, ISIJ Int. 56 (2016) 24–36. https://doi.org/10.2355/isijinternational.ISIJINT-2015-430.

[62] J.Y. Lee, J.L. Lee, J.L. Lee, A trapping theory of hydrogen in pure iron, Philos. Mag. A Phys. Condens. Matter, Struct. Defects Mech. Prop. 56 (1987) 293–309. https://doi.org/10.1080/01418618708214387.

[63] W.Y. Choo, J.Y. Lee, Thermal Analysis of Trapped Hydrogen in Pure Iron, 13 (1982) 423–427.

[64] M. Enomoto, D. Hirakami, T. Tarui, Modeling thermal desorption analysis of hydrogen in steel, ISIJ Int. 46 (2006) 1381–1387. https://doi.org/10.2355/isijinternational.46.1381.

[65] H. Hagi, Effect of interface between cementite and ferrite on diffusion of hydrogen in carbon steels, Mater. Trans. JIM. 35 (1994) 168–173. https://doi.org/10.2320/matertrans1989.35.168.

[66] I. Maroef, D.L. Olson, M. Eberhart, G.R. Edwards, Hydrogen trapping in ferritic steel weld metal, Int. Mater. Rev. 47 (2002) 191–223. https://doi.org/10.1179/095066002225006548.

[67] A.J. Haq, K. Muzaka, D.P. Dunne, A. Calka, E. V. Pereloma, Effect of microstructure and composition on hydrogen permeation in X70 pipeline steels, Int. J. Hydrogen Energy. 38 (2013) 2544–2556. https://doi.org/10.1016/j.ijhydene.2012.11.127.

[68] C.F. Dong, Z.Y. Liu, X.G. Li, Y.F. Cheng, Effects of hydrogen-charging on the susceptibility of X100 pipeline steel to hydrogen-induced cracking, Int. J. Hydrogen Energy. 34 (2009) 9879–9884. https://doi.org/10.1016/j.ijhydene.2009.09.090.

[69] Q. Liu, J. Venezuela, M. Zhang, Q. Zhou, A. Atrens, Hydrogen trapping in some advanced high strength

steels, Corros. Sci. 111 (2016) 770–785. https://doi.org/10.1016/j.corsci.2016.05.046.

[70]   P. Zhou, W. Li, H. Zhao, X. Jin, Role of microstructure on electrochemical hydrogen permeation properties in advanced high strength steels, Int. J. Hydrogen Energy. 43 (2018) 10905–10914. https://doi.org/10.1016/j.ijhydene.2018.04.241.

[71]   C. Moriconi, Modélisation de la propagation de fissure de fatigue assistée par l'hydrogène gazeux dans les matériaux métalliques (in French), PhD Thesis, ENSMA, Poitiers, France, 2013.

[72]   S. Serebrinsky, E.A. Carter, M. Ortiz, A quantum-mechanically informed continuum model of hydrogen embrittlement, J. Mech. Phys. Solids. 52 (2004) 2403–2430. https://doi.org/10.1016/j.jmps.2004.02.010.

[73]   I. Scheider, W. Brocks, Simulation of cup - cone fracture using the cohesive model, Eng. Fract. Mech. 70 (2003) 1943–1961. https://doi.org/10.1016/S0013-7944(03)00133-4.

[74]   G. Gobbi, C. Colombo, S. Miccoli, L. Vergani, A weakly coupled implementation of hydrogen embrittlement in FE analysis, Finite Elem. Anal. Des. 141 (2018). https://doi.org/10.1016/j.finel.2017.11.010.

[75]   E.D. Hondros, M.P. Seah, Theory of Grain Boundary Segregation in Terms of Surface Adsorption Analogues., Met. Trans A. 8 A (1977) 1363–1371. https://doi.org/10.1007/BF02642850.

[76]   A. Van der Ven, G. Ceder, Impurity-induced van der Waals transition during decohesion, Phys. Rev. B - Condens. Matter Mater. Phys. 67 (2003). https://doi.org/10.1103/PhysRevB.67.060101.

[77]   L.B. Peral, A. Zafra, S. Blasón, C. Rodríguez, J. Belzunce, Effect of hydrogen on the fatigue crack growth rate of quenched and tempered CrMo and CrMoV steels, Int. J. Fatigue. 120 (2019) 201–214. https://doi.org/10.1016/j.ijfatigue.2018.11.015.

[78]   M.L. Martin, M. Dadfarnia, A. Nagao, S. Wang, P. Sofronis, Enumeration of the hydrogen-enhanced localized plasticity mechanism for hydrogen embrittlement in structural materials, Acta Mater. 165 (2019) 734–750. https://doi.org/10.1016/j.actamat.2018.12.014.

[79]   K.-H. Schwalbe, I. Scheider, A. Cornec, Guidelines for applying cohesive models to the damage behaviour of engineering materials and structures, Springer-Verlag, Berlin Heidelberg, 2013. https://doi.org/10.1007/978-3-642-29494-5.

[80]   K.H. Schwalbe, Introduction of δ5 as an operational definition of the CTOD and its practical use, in: W.G. Reuter, J.H. Underwood, J.C. Newman (Eds.), ASTM Spec. Tech. Publ., American Society for Testing and Materials, Philadelphia (PA), 1995: pp. 763–778.

[81]   D.C. Ahn, P. Sofronis, R. Dodds, Modeling of hydrogen-assisted ductile crack propagation in metals and alloys, Int. J. Fract. 145 (2007) 135–157. https://doi.org/10.1007/s10704-007-9112-3.

[82]   G. Gobbi, C. Colombo, L. Vergani, Sensitivity analysis of a 2D cohesive model for hydrogen embrittlement of AISI 4130, Eng. Fract. Mech. 167 (2016). https://doi.org/10.1016/j.engfracmech.2016.03.045.

[83]   C. Colombo, G. Fumagalli, F. Bolzoni, G. Gobbi, L. Vergani, Fatigue behavior of hydrogen pre-charged low alloy Cr-Mo steel, Int. J. Fatigue. 83 (2015) 2–9. https://doi.org/10.1016/j.ijfatigue.2015.06.002.

[84]   G. Álvarez, L.B. Peral, C. Rodríguez, T.E. García, F.J. Belzunce, Hydrogen embrittlement of structural steels: Effect of the displacement rate on the fracture toughness of high-pressure hydrogen pre-charged samples, Int. J. Hydrogen Energy. 44 (2019) 15634–15643. https://doi.org/10.1016/j.ijhydene.2019.03.279.

[85]   G. Juilfs, Das Diffusionsverhalten von Wasserstoff in einem niedriglegierten Stahl unter Berücksichtigung des Verformungsgrades, TU Hamburg, Hamburg, 2001.

[86] X. Li, J. Zhang, Y. Wang, M. Ma, S. Shen, X. Song, The dual role of shot peening in hydrogen-assisted cracking of PSB1080 high strength steel, Mater. Des. 110 (2016) 602–615. https://doi.org/10.1016/j.matdes.2016.07.121.

[87] X. Li, J. Zhang, M. Ma, X. Song, Effect of shot peening on hydrogen embrittlement of high strength steel, Int. J. Miner. Metall. Mater. 23 (2016) 667–675. https://doi.org/10.1007/s12613-016-1279-z.
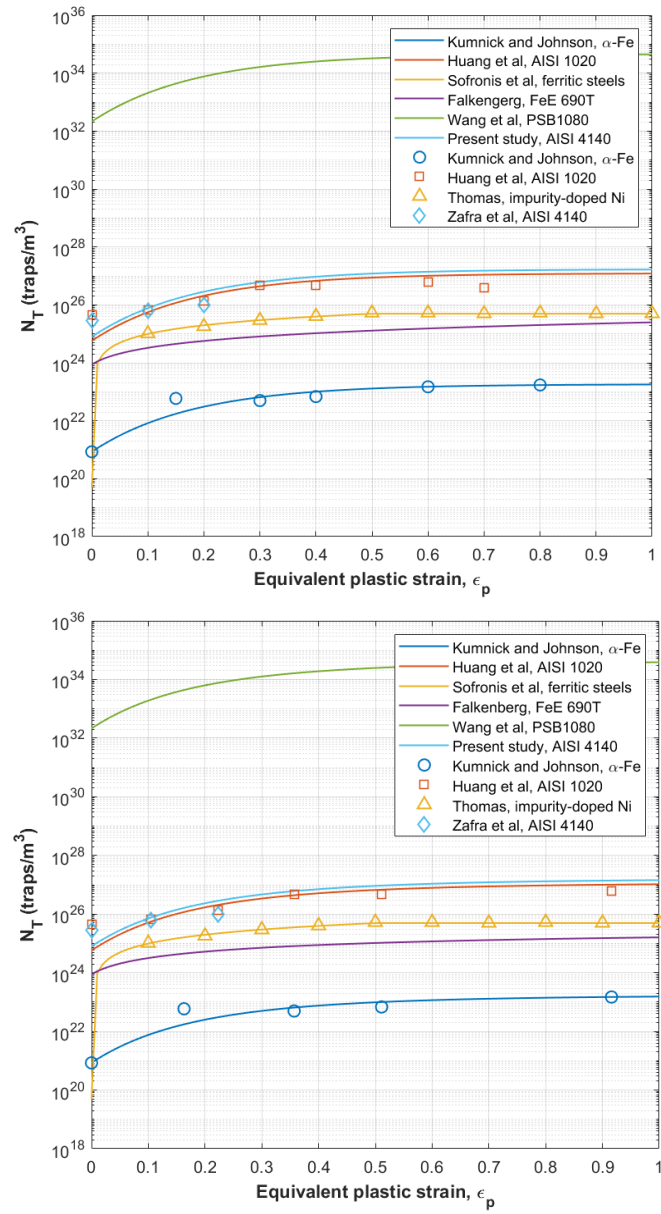
Figures

Figure 1: Trap density N_T as a function of the equivalent plastic strain ε_p.
Reference works for the analytical laws are: Kumnick and Johnson [43], Huang et al. [44], Sofronis et al. [47], Wang et al. [46].
Reference works for the experimental data are: Kumnick and Johnson [43], Huang et al. [44], Thomas [48], Zafra [51].
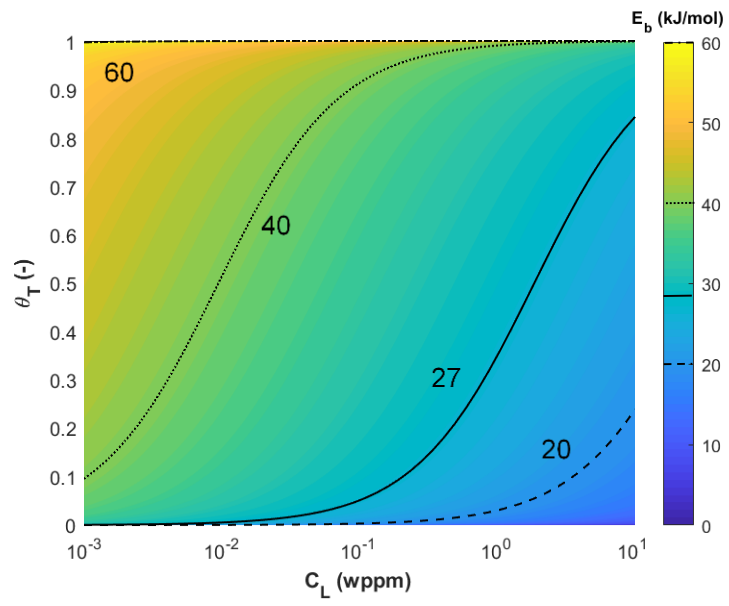
Figure 2: Trap occupancy θ_T as a function of lattice concentration C_L, and of different binding energies E_b.
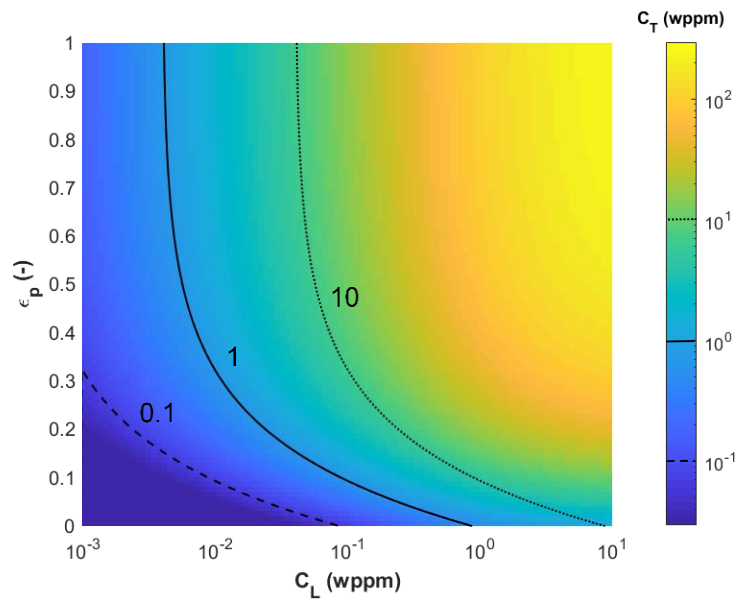
Figure 3: Hydrogen concentration in traps, C_T, as a function of lattice concentration, C_L, and equivalent plastic strain, ε_p. Concentrations C_T and C_L are in logarithmic scale. The plot corresponds to a constant $E_b=27kJ/mol$.
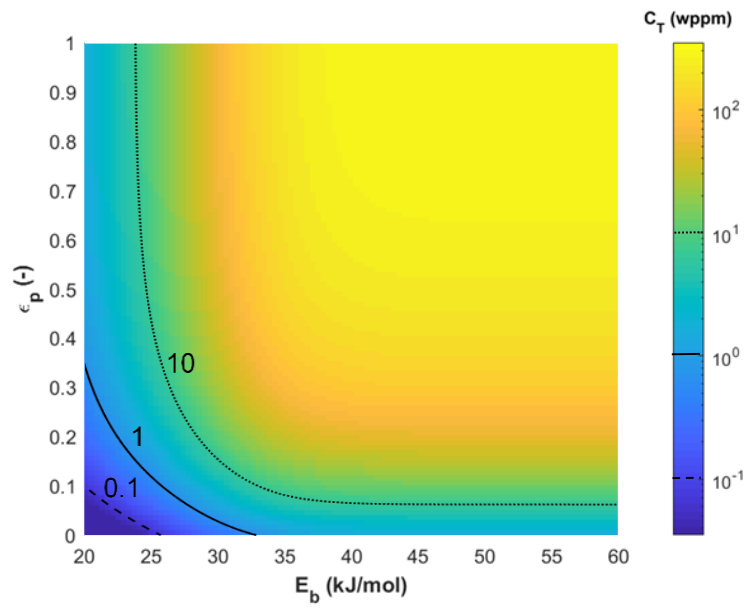
Figure 4: Hydrogen concentration in traps, C_T, as a function of binding energy, E_b, and equivalent plastic strain, ε_p. Concentration C_T is in logarithmic scale. The plot corresponds to a constant C_L=0.150wppm.
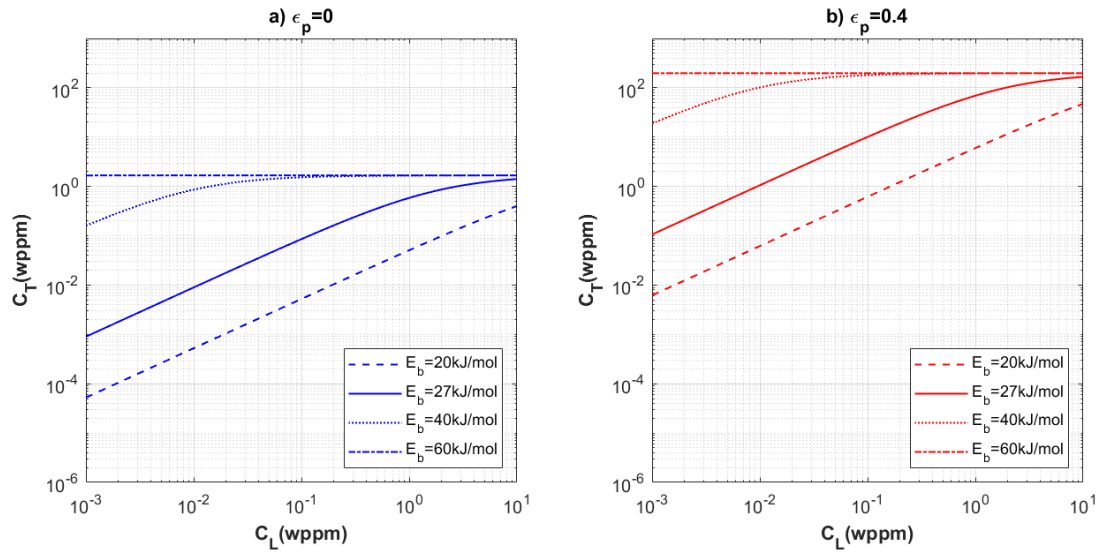
Figure 5: Hydrogen concentration in traps, C_T, as a function of lattice concentration, C_L, for different binding energies E_b. Plots are given for: a) ε_p=0; b) ε_p=0.4. The solid line, corresponding to E_b=27kJ/mol, will be taken as a reference in the present study, based on the work [51].
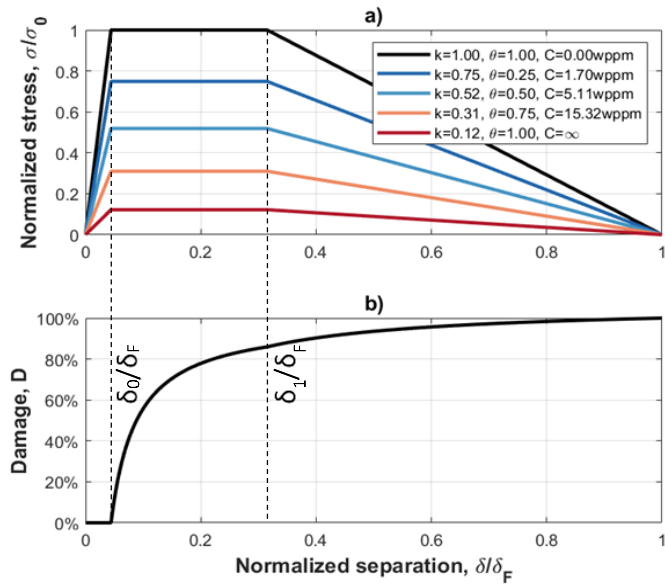
Figure 6: Law for cohesive elements: a) normalized trapezoidal Traction Separation law (TSL), i.e. σ/σ₀ vs δ/δ_F; and b) damage vs. normalized separation. Trends of normalized stress are given as a function of the decreasing factor k, of the hydrogen coverage θ, and of the total hydrogen concentration C, to account for hydrogen effect.
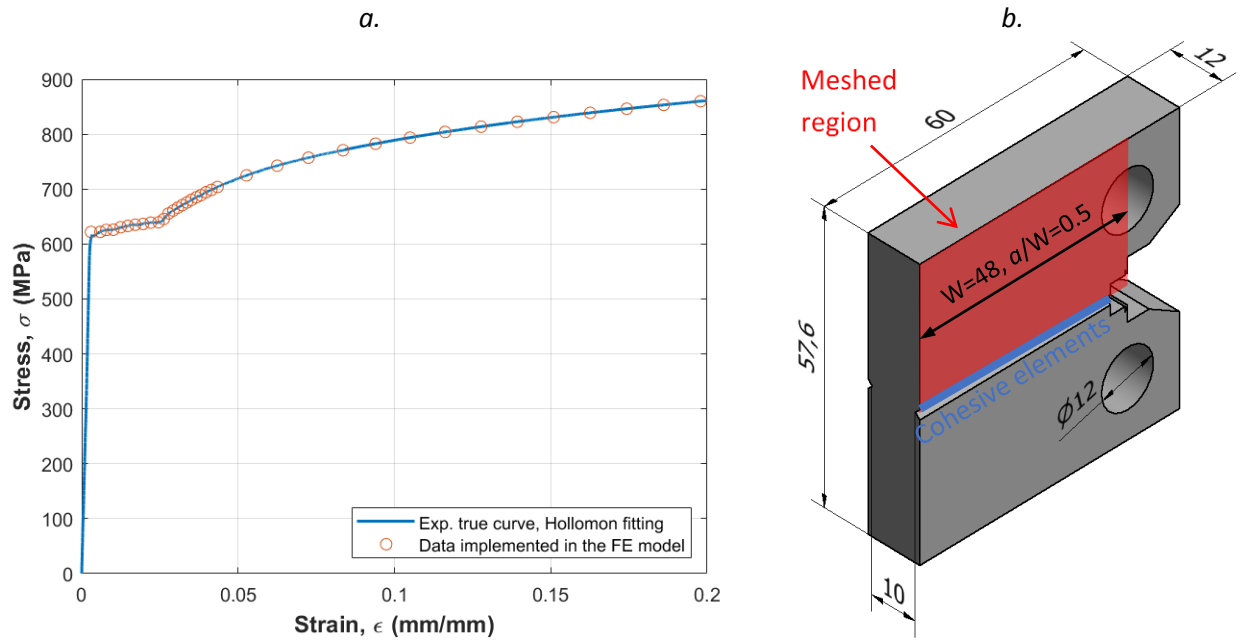
Figure 7: a) Experimental true stress-strain curve obtained from uniaxial tensile tests on AISI 4140 steel quenched and tempered at 700ºC [24]*, and data selected for the implementation in the numerical model; b) Geometry of the C(T) specimens with sizes in mm.*
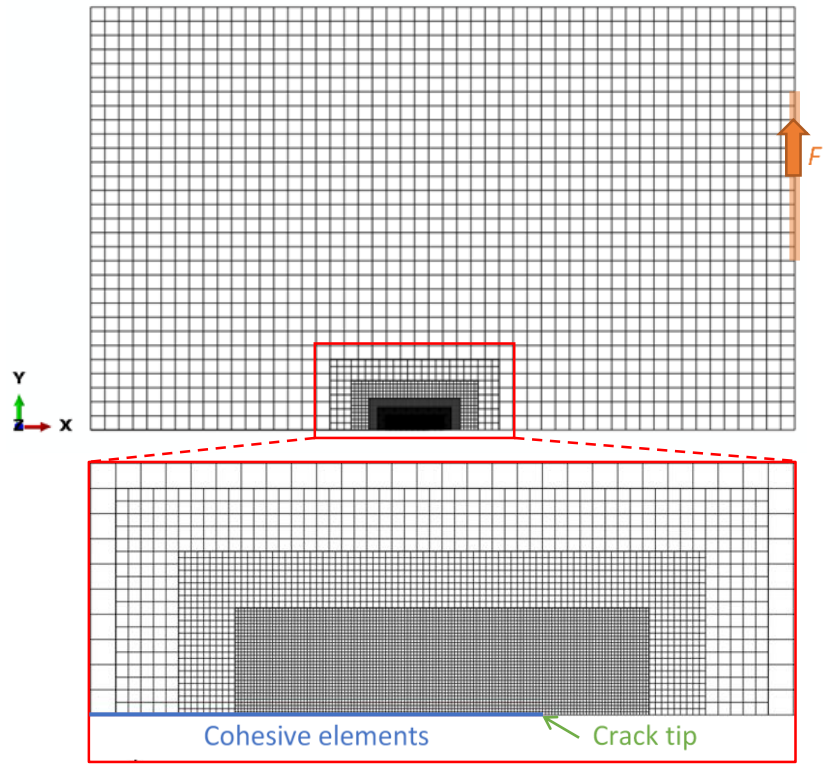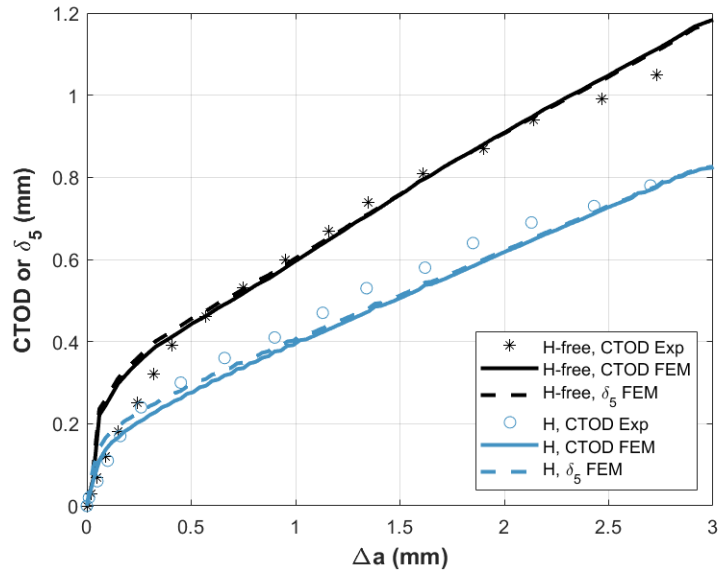
Figure 8: Details of the mesh for the C(T) specimen.

Figure 9: Comparison between numerical (FEM) and experimental (Exp) data without and with hydrogen. R-curve: Crack Tip Opening Displacement (CTOD) and its estimation δ₅ according to [80] as a function of the crack growth, Δa.
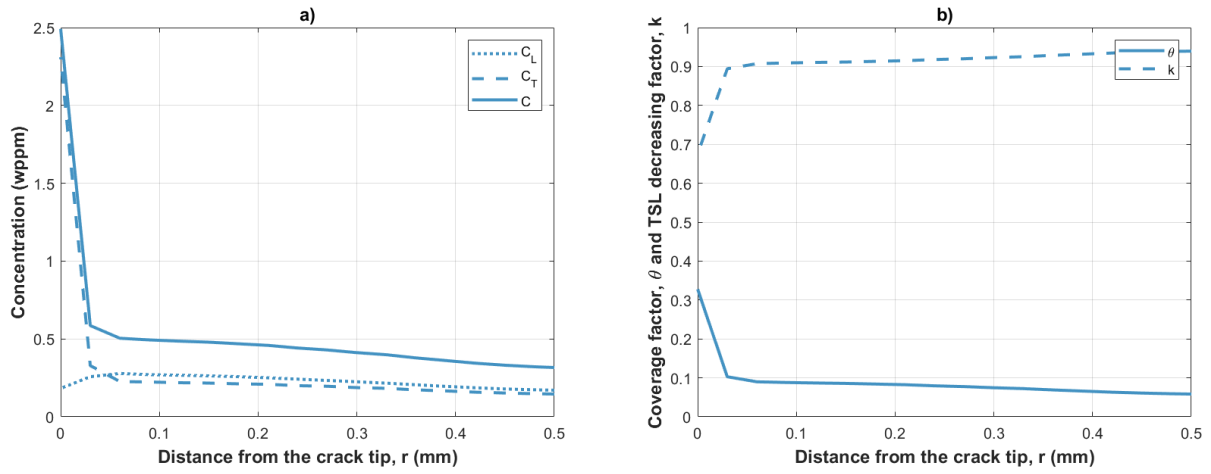
Figure 10: Trends of: a) hydrogen concentration in lattice, C_L, in traps, C_T, and total hydrogen concentration, C; b) coverage factor θ and decreasing factor k, as a function of the distance from the crack tip. The time increment corresponds to the onset of crack propagation, i.e. when the first cohesive element at the crack tip is fully damaged with D=100%.
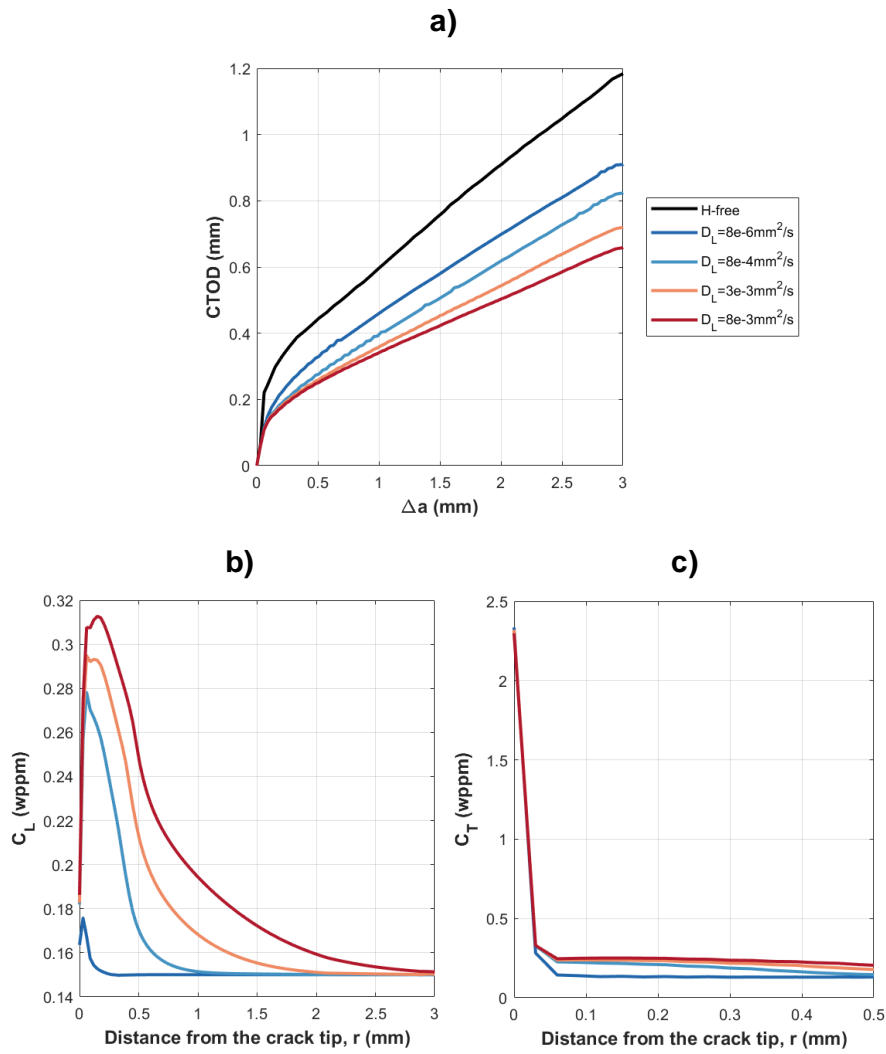
Figure 11: Sensitivity analysis for the diffusion coefficient D_L. Plots of: a) CTOD R-curve; b) C_L and c) C_T as a function of the distance from the crack tip, at the onset of crack propagation.
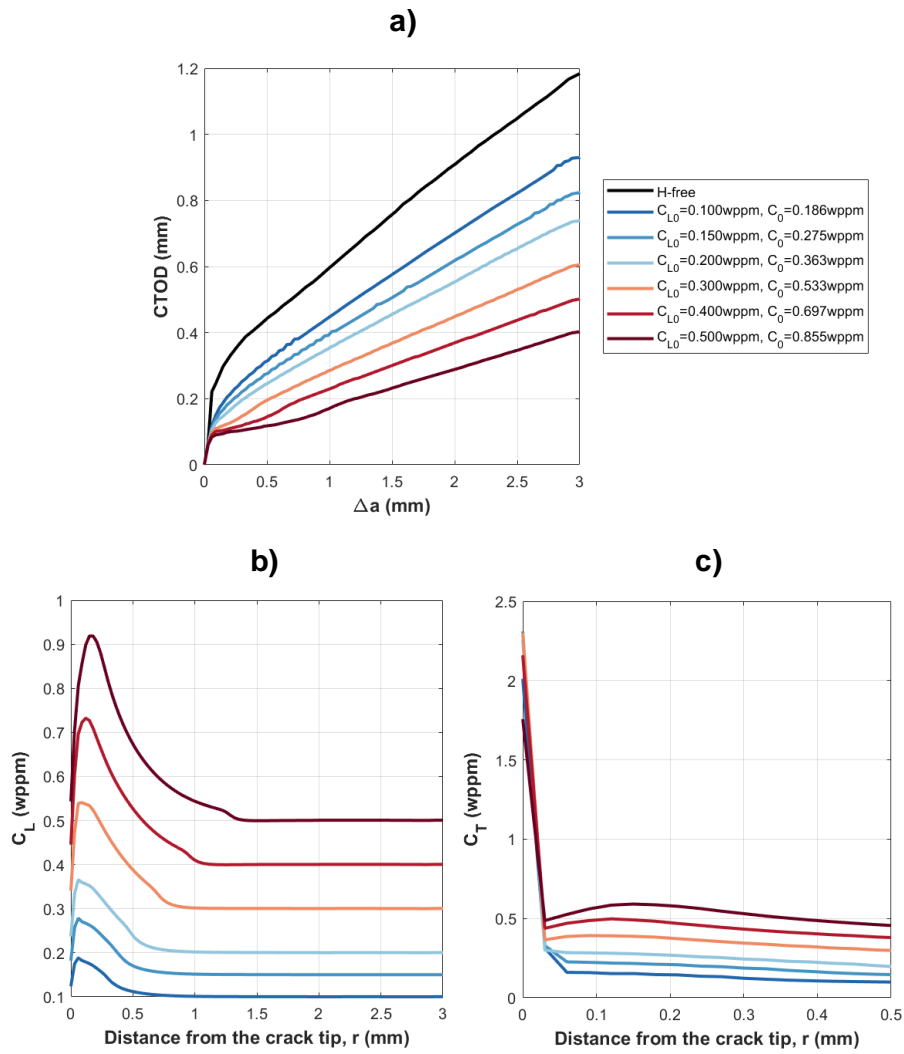
Figure 12: Sensitivity analysis for the hydrogen concentrations C_L and C. Plots of: a) CTOD R-curve; b) C_L and c) C_T as a function of the distance from the crack tip, at the onset of crack propagation.

a)

b)   **c)**

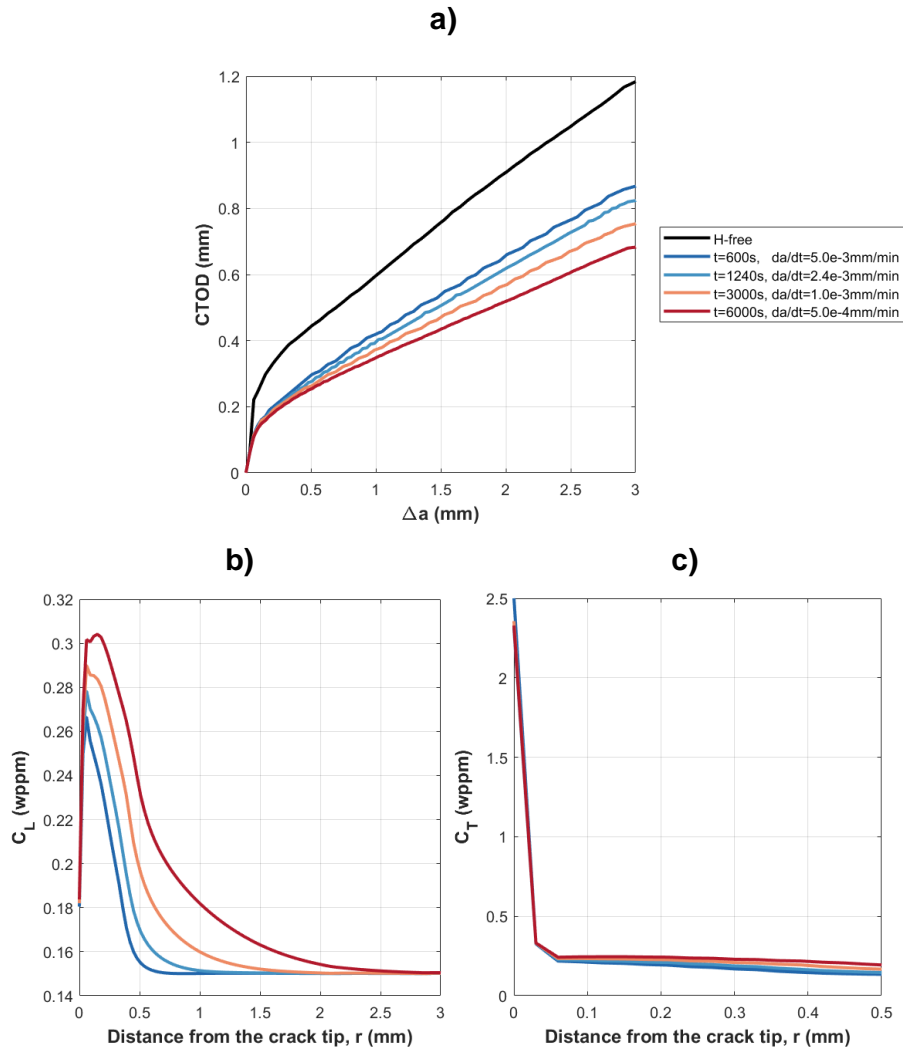*Figure 13: Sensitivity analysis for the time, t, to reach Δa=3mm. Plots of: a) CTOD R-curve; b) C_L and c) C_T as a function of the distance from the crack tip, at the onset of crack propagation.*

Tables

Table 1: Summary of literature equations for the estimation of trap density N_T as a function of the equivalent plastic strain ε_p.

Authors	Material	Interpolating equation	Ref.	Ref. of exp. data
Kumnick, Johnson (1980)	α-Fe	$log\, N_T = 23.26 - 2.33\, exp\left(-5.5\varepsilon_p\right)$	[43]	[43]
Huang, Shaw (1995)	AISI 1020	$log\, N_T = 27.15 - 2.33\, exp\left(-5.5\varepsilon_p\right)$	[44]	[44]
Sofronis et al. (2001)	Ferritic steels	$N_T = \sqrt{2}\dfrac{\bar{\rho}}{\bar{a}}$ $\quad$ where $\bar{\rho} = \begin{cases} \bar{\rho}_0 + \gamma\varepsilon_p & for\ \varepsilon_p \leq 0 \\ \bar{\rho}_1 & for\ \varepsilon_p \geq 0 \end{cases}$ and $\bar{\rho}_0 = 10^{10}\, line\, length/m^3$ dislocation density for annealed material with $\varepsilon_p = 0$; $\bar{\rho}_1 = 10^{16}m/m^3$ maximum dislocation density; $\gamma = 2 \cdot 10^{16}\, line\, length/m^3$	[47]	[48]
Falkenberg (2010)	FeE 690T	$log\, N_T = 23.94 + 24.68 \cdot \varepsilon_p^{0.7}$	[45]	[85]
Wang et al. (2018)	PSB1080 (peened)	$log\, N_T = 34.66 - 2.33\, exp\left(-5.5\varepsilon_p\right)$	[46]	[86,87]
Present study	AISI 4140	$log\, N_T = 27.23 - 2.33\, exp\left(-5.5\varepsilon_p\right)$	This study	[51]

Table 2: TSL parameters, obtained from trial and error calibration, comparing numerical CTOD-Δa (or δ_5-Δa) curves with experimental data without hydrogen [19].

δ_0 (mm)	δ_1 (mm)	δ_F (mm)	σ_0 (MPa)	σ_0/YS
1.1e-3	9.0e-3	3.0e-2	2200	3.54